

Experimental estimation of seismic properties of new precast shear wall spatial structure model

Wu Dongyue^{a,*}, Liang Shuting^b, Shen Mengying^c, Guo Zhengxing^b, Zhu Xiaojun^d, Sun Chongfang^e

^a School of Civil Engineering and Architecture, Jiangsu University of Science and Technology, Zhenjiang, Jiangsu, China

^b School of Civil Engineering, Southeast University, Nanjing, Jiangsu, China

^c Zhenjiang Archives, Zhenjiang, Jiangsu, China

^d Architects and Engineers Co., Ltd, Southeast University, Nanjing, Jiangsu, China

^e Jinan Rail Transit Group Co., Ltd, Jinan, Shandong, China

ARTICLE INFO

Keywords:

Precast
Shear wall
Grouted connection
Seismic performance
Spatial model

ABSTRACT

Effective seismic properties are a basic requirement in precast shear wall applications. Therefore, this study focuses on the evaluation and improvement of precast shear wall seismic properties using the new pore-forming grouted connector with welded closure confinement steels (NPGCS) developed in previous research. The NPGCS connector reliability was verified and the seismic properties of the NPGCS spatial structure model were evaluated by carrying out a low cyclic reversed lateral loads experimental test on the NPGCS precast shear wall spatial structure model containing superposed connecting beams and precast shear walls, which were selected from a practical high-rise precast residential building. According to the testing results of the crack distribution and component failure modes, the superposed connecting beam properties were weak, and damaged early in the shear failure mode, while the precast shear walls cracked after the steel bars in the superposed connecting beams yielded. Furthermore, the failure mode indicated that the NPGCS connection applied in this spatial model is reliable, while two new weak sections were proven to exist at the connector ends. Together with the precast joint interface slip, the dowel shear action is demonstrated to be harmful to the joint interface properties. Additional seismic parameters, namely capacity, ductility, stiffness and energy consumption, were used to complete the evaluation of the seismic properties of the NPGCS spatial structure model. Overall, although the NPGCS spatial model ductility is low, the strengths are high, leading to continued effective energy consumption properties, which indicates favourable seismic properties of the NPGCS spatial structural model.

1. Introduction

Precast technologies have made substantial advances in industrial production, environmental protection and high mechanical reliability, among others. However, precast technologies are still limited in terms of extensive application in China, for the two following reasons: (1) as most Chinese territories are in seismic areas, stricter seismic design requirements exist; and (2) owing to the high population density in south-eastern China, most Chinese residential buildings are high-rise shear wall structures with 20 to 33 floors, which drastically enlarge the seismic loads [1].

In recent years, numerous new types of steel bar connectors [4–12] and testing technologies [13–16] have been developed based on grouted connectors [2] and inherited from the Precast Seismic Structural System (PRESS) programme connectors [3]. Figs. 1 and 2 depict two typical grouted connectors that are widely used in China. Although

these new grouted precast connectors are capable of providing very high connector performance, special manufacturing technologies are required, such as stressing in unbounded pre-stressed connectors [17] and steel sleeves in grouted connectors. All of these special manufacturing technologies will increase the cost and dramatically limit the application of precast technologies.

Understanding the connecting mechanisms is a very basic necessity for reducing manufacturing costs while achieving effective connection properties. Early research on grouted steel sleeve connectors [18,19] already proved that steel bar embedded situations and confinements determine the connector properties. Steel bar embedded situations include the embedded length, steel bar surface and anchor situations. Confinements are usually generated by confinement steel bars or steel sleeves. Early research on non-sleeve grouted connectors, which were developed in recent years and offer increased economic advantages [6–7,10], indicated that although the steel bar embedded length was

* Corresponding author.

E-mail addresses: dywu@just.edu.cn (D. Wu), stliang@seu.edu.cn (S. Liang).

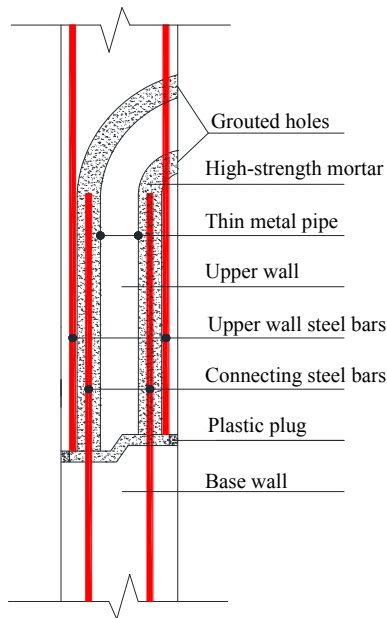


Fig. 1. Zhongnan NPC grouted connector technology.

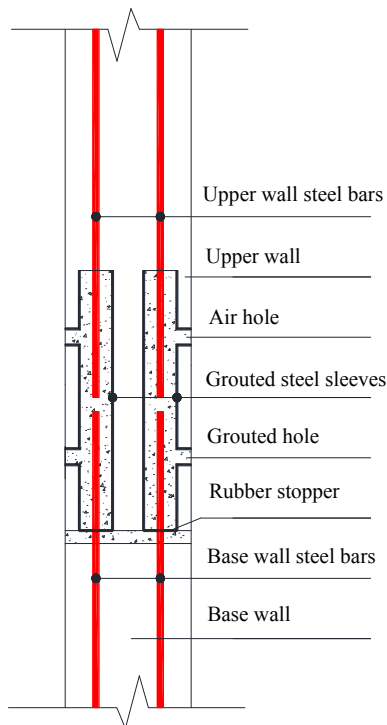


Fig. 2. Steel sleeve grouted connector.

longer than that in the grouted steel sleeve connector and several steel anchor types were also used, the connecting properties were unable to reach those of cast-in-situ continuous steel bars. The reason for this relates to confinements: steel sleeves have a thick steel outer wall and small diameter, which can easily provide a strong confinement stress on the grouted material and enable the tensile stress to transfer effectively onto the overlapped steel bars, while the new non-sleeve connectors neglect the confinement effects. Therefore, the research perfectly



Fig. 3. Welded confinement steel hoop.

illustrated that confinement is another key factor for grouted connectors.

According to the research conclusions from Moosavi [20] and Saatcioglu [21], in order to generate sufficient confinement stress, the confinement steel bar diameter, strength, steel bar hoop size and vertical distance should be reasonably considered. Therefore, a new and low-cost NPGCS connector (a new pore-forming grouted connector with welded closure confinement steels) was invented in early studies in order to simplify the precast connector manufacturing and achieve strong connection properties [22]. This was accomplished by adopting the following approaches: (1) using a welded confinement steel hoop joint to improve the single steel bar hoop strength; (2) buckling the configured confinement steel hoops to a low steel hoop size and generating a superposed confinement area; and (3) reducing the vertical distance for confinement steel hoops.

In early experimental research on NPGCS, its connection reliability was proven [7,12]. However, in high-rise residential precast shear wall buildings, the precast shear walls bear a higher seismic load and work together with the connecting beams formed by the shear wall window openings. Therefore, the seismic performance of the NPGCS shear wall combined with connecting beams should also be considered. In this study, an experimental evaluation was carried out on one NPGCS spatial structure model containing precast shear wall and superposed connecting beam components.

2. Test background

2.1. Npgcs

The NPGCS only uses the widely applied normal steel bars and pre-buried thin metal pore to replace the expensive grouted steel sleeve and reduce manufacturing costs. The NPGCS is composed of buckle-configured confinement steel bar hoops, connecting overlapped steel bars, a thin metal pore and grouting materials. Fig. 3 illustrates a welded confinement steel hoop produced by an automatic welding production line, while Fig. 4 depicts the NPGCS steel bar configuration. In contrast to the traditional grouted connectors, the NPGCS offers the advantages of superior confinement conditions and easier manufacturing [7,12].

2.2. Design criteria for NPGCS connector

There are three basic design criteria for the NPGCS, as follows.

- (1) Welded strength of closure confinement steel bar hoops: as the welded closure confinement steel bar hoops play a key role as steel sleeves, the arc butt welding approach is utilised, and the tension strength of the welded joint should be no less than that of a single

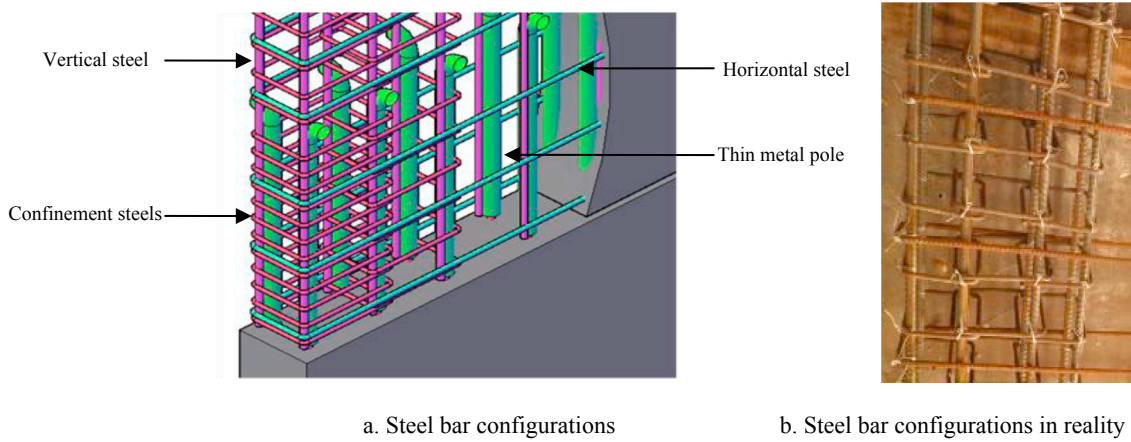


Fig. 4. NPGCS steel bar configurations.

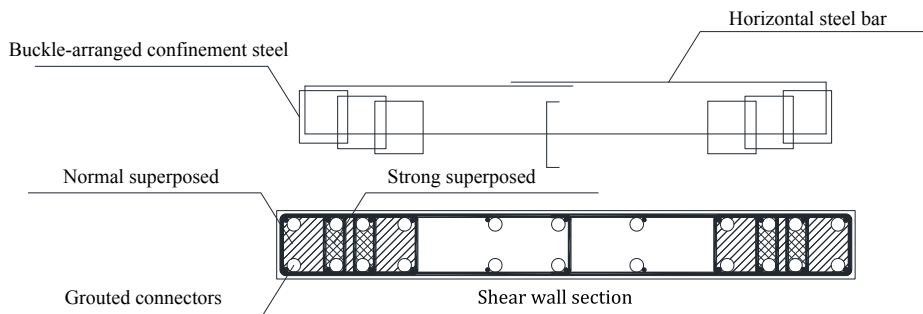
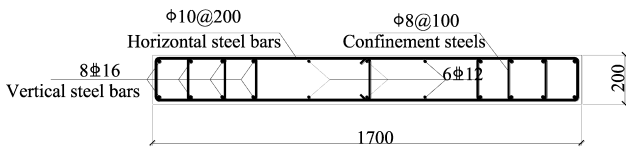
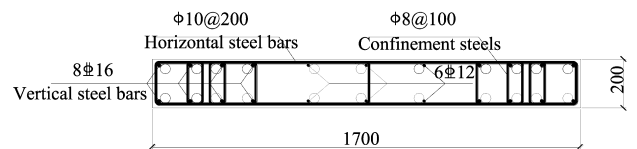


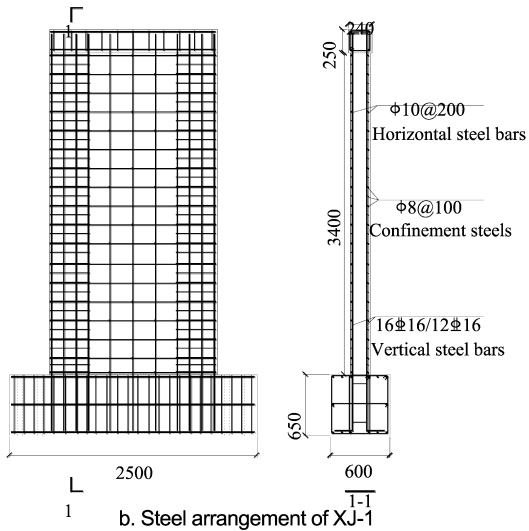
Fig. 5. Buckle-arranged confinement steel hoops and superposed area.



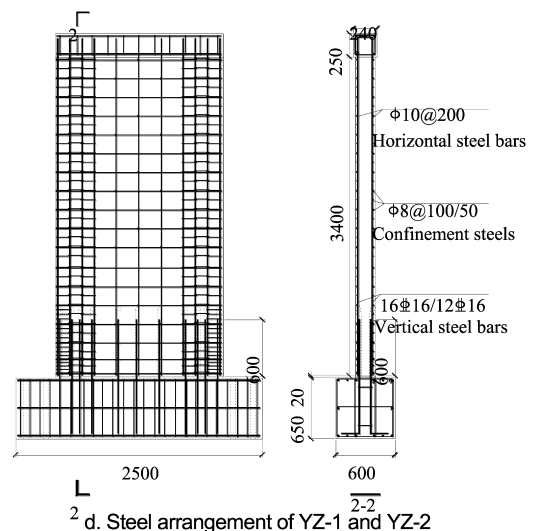
a. Cross-section of XJ-1



c. Cross-section of YZ-1 and YZ-2



b. Steel arrangement of XJ-1



d. Steel arrangement of YZ-1 and YZ-2

Fig. 6. Specimen sizes and steel configurations (mm).

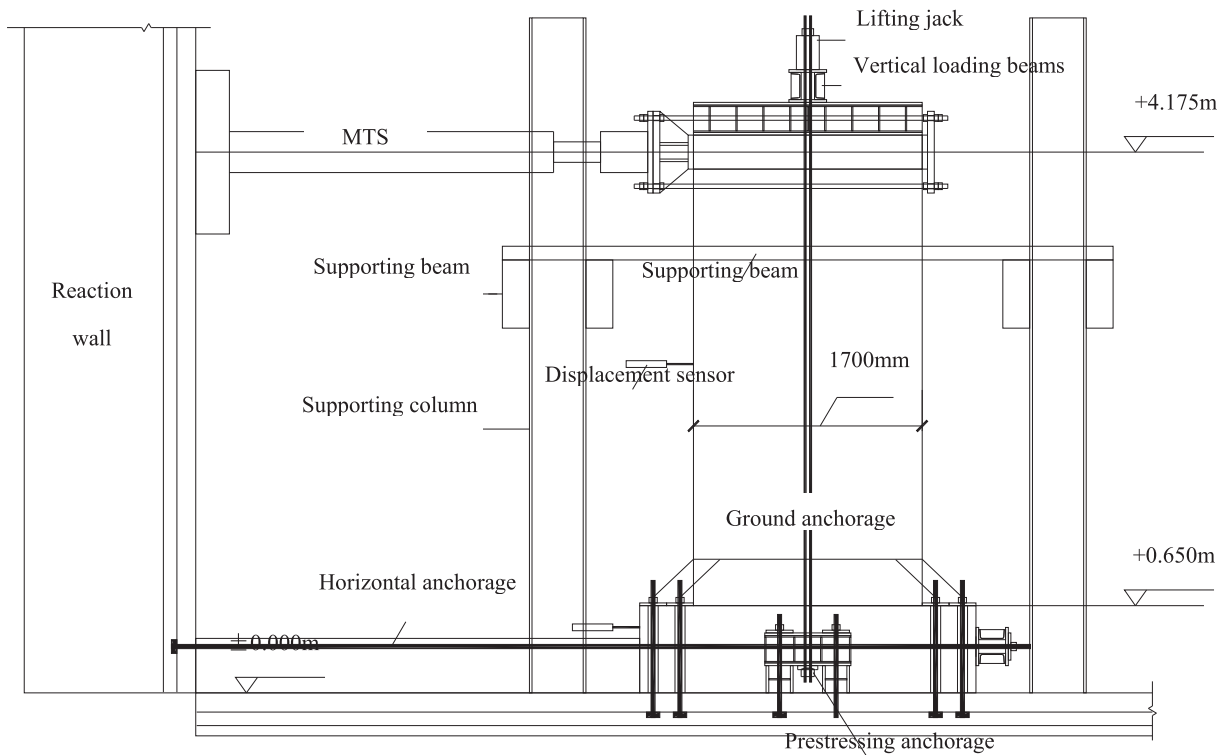


Fig. 7. Test setup.

Table 1
Specimen sizes and test results.

Specimen	Height × width × thickness (mm)	Joint connector	Crack strength (kN)	Yield strength (kN)	Ultimate strength (kN)	Yield displacement (mm)	Ultimate displacement (mm)	Ductility coefficient μ
XJ-1	3400 × 1700 × 200	Cast-in-situ	200	320	580	15	90	6
ZP-1	3400 × 1700 × 200	NPGCS for 8 Φ 16 + 6 Φ 12	200	340	605	18.5	92.5	5
ZP-2	3400 × 1700 × 200	NPGCS for 8 Φ 16 + 6 Φ 12	200	320	598	17.8	106.8	6



a. XJ-1

b. ZP-1

c. ZP-2

Fig. 8. Failure of cast-in-situ and NPGCS precast shear wall specimens.

continuous steel bar with the same strength grade and diameter.

(2) Buckle configuration of confinement steel hoops: to provide sufficient confinement stress. The buckle steel hoop configuration requires the adjacent welded closure confinement steel hoops to

buckle one another in the horizontal direction. As a result, the adjacent two confinement steel hoops will generate a strong superposed area, and the grouting connectors contained in this area will bear a larger confinement stress (as illustrated in Fig. 5).

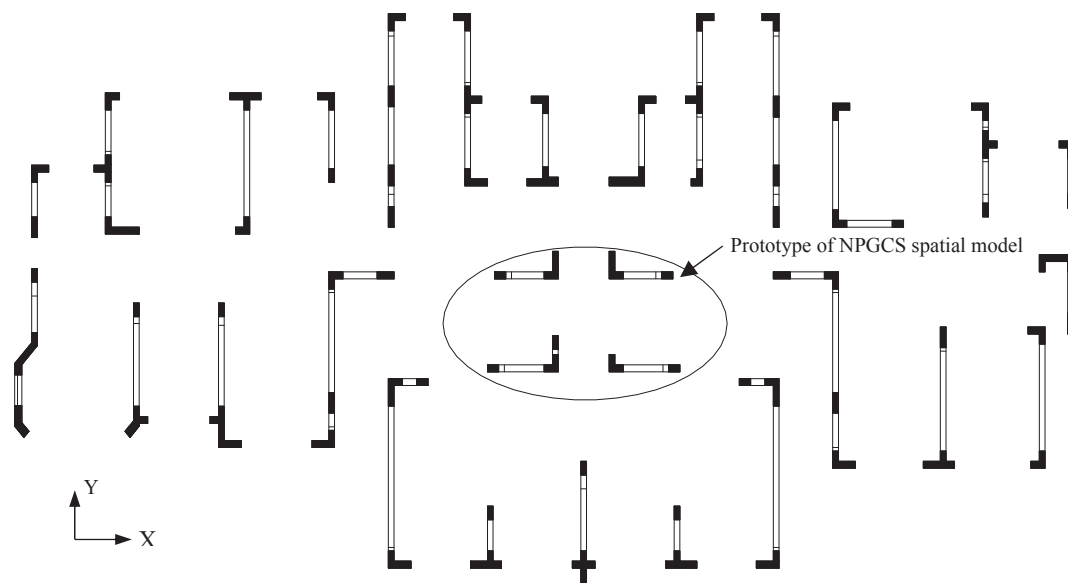


Fig. 9. NPGCS spatial model prototype on key floor.

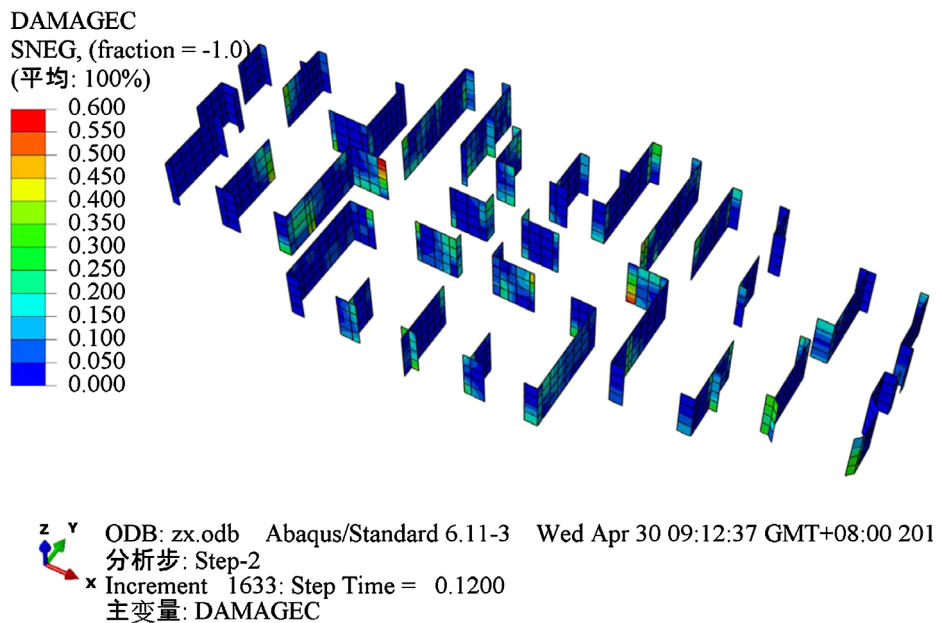
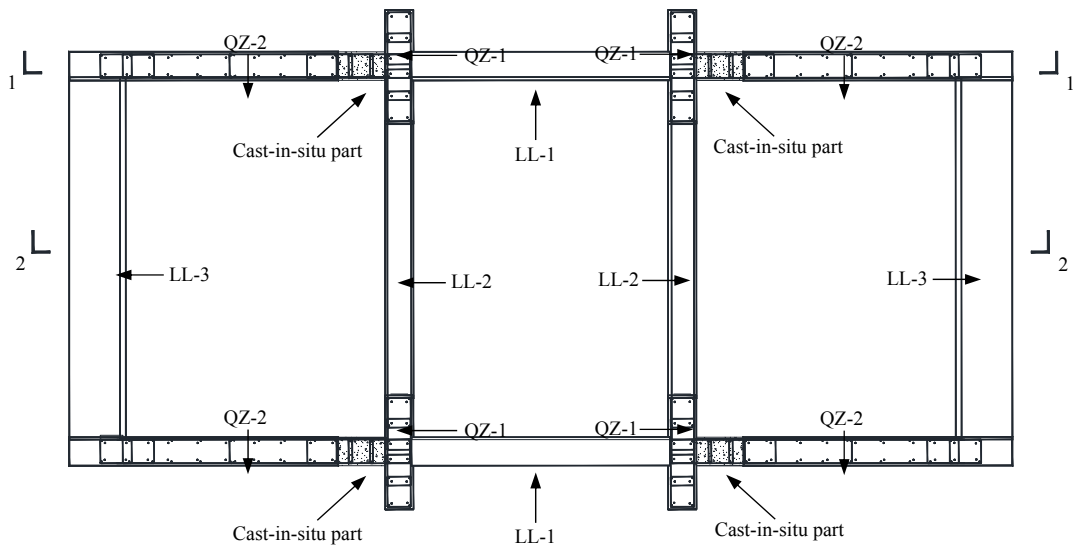


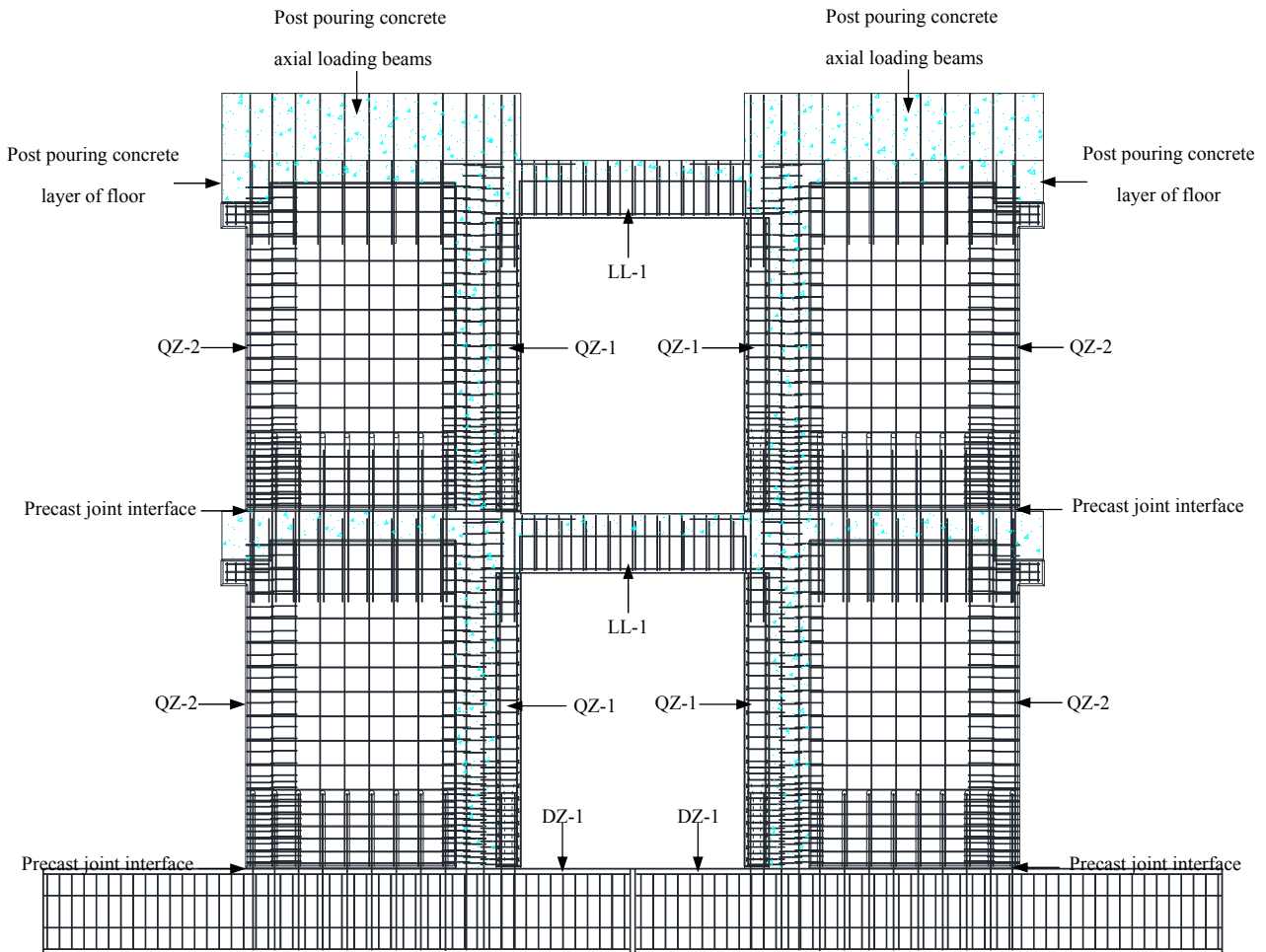
Fig. 10. Concrete compressive damage of vertical shear walls on key floor.

Table 2
Sizes and steel bars in NPGCS spatial model components (mm).

Component number	Component name	Component sizes (height × width × thickness)	Vertical steel	Horizontal/confinement steel
QZ-1	Flange of T-section shear wall	1190 × 400 × 100	12Φ6 mm	Φ6@100 mm
QZ-2	Web of T-section shear wall	1340 × 850 × 100	8Φ6 + 10Φ6 mm	Φ6@100 mm
DZ-1/2	Experimental loading base	2390 × 900 × 350	36Φ4 mm	Φ8@50 mm
LL-1	Longitudinal superposed connecting beam	150 × 100 × 920	3Φ8 mm	Φ6@50 mm
LL-2	Inside transverse superposed connecting beam	100 × 100 × 970	3Φ12 mm	Φ6@50 mm
LL-3	Outside transverse superposed connecting beam	100 × 200 × 1270	3Φ12 mm	Φ6@50 mm
DB-1/2	Superposed slab	50 × 945 × 1270	Φ6@100 mm	Φ6@100 mm

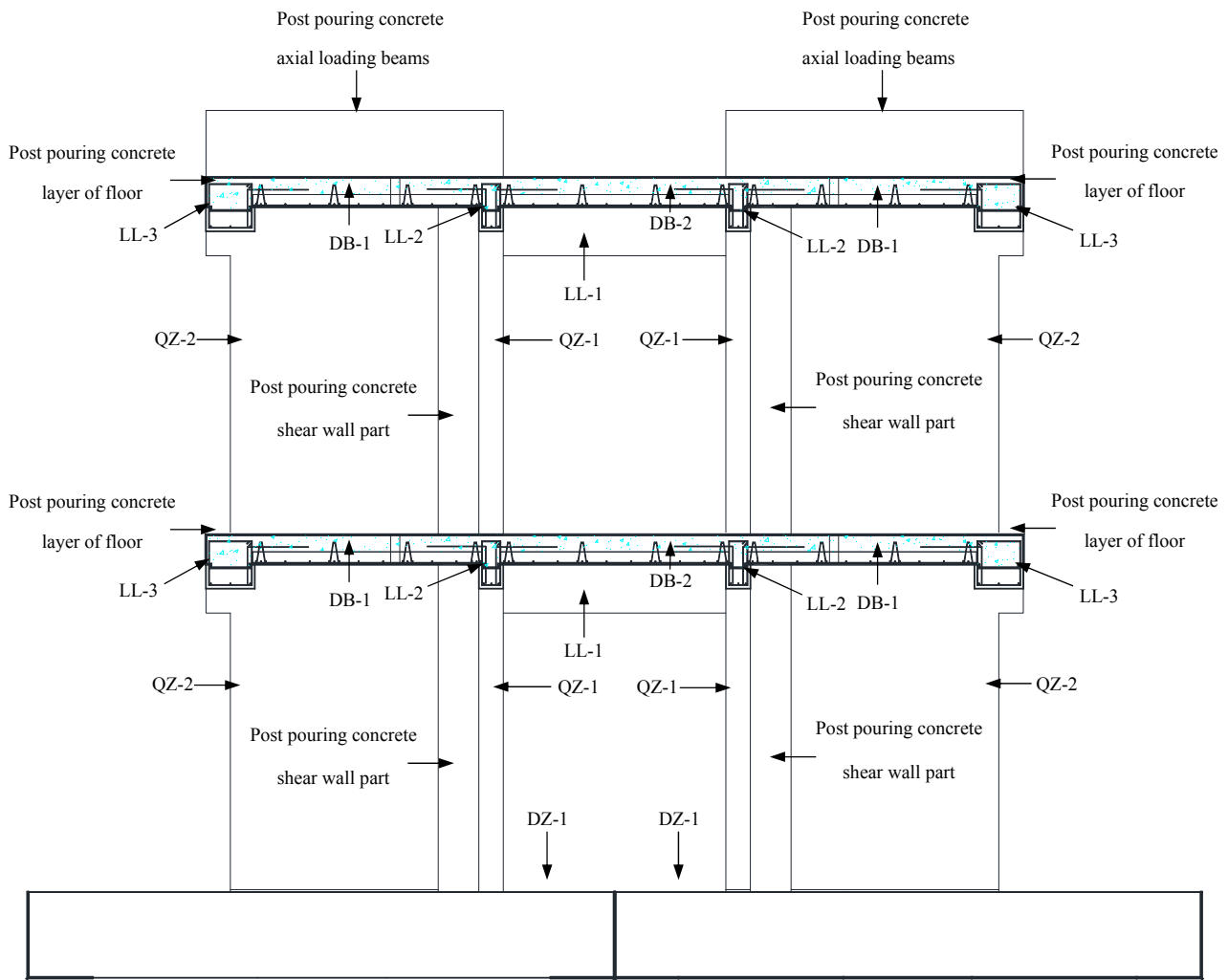


a. Components of NPGCS spatial model in plan



b. 1-1 sectional view of NPGCS spatial model

Fig. 11. Assembly details of NPGCS spatial model.



c. 2-2 sectional view of NPGCS spatial model

Fig. 11. (continued)

(3) In the vertical direction, the confinement steel hoops in the shear wall marginal area will be strengthened by reducing the adjacent confinement steel hoop distance by half. The excessive steel bar hoops with a small distance will be able to supply a sufficiently strong confinement stress.

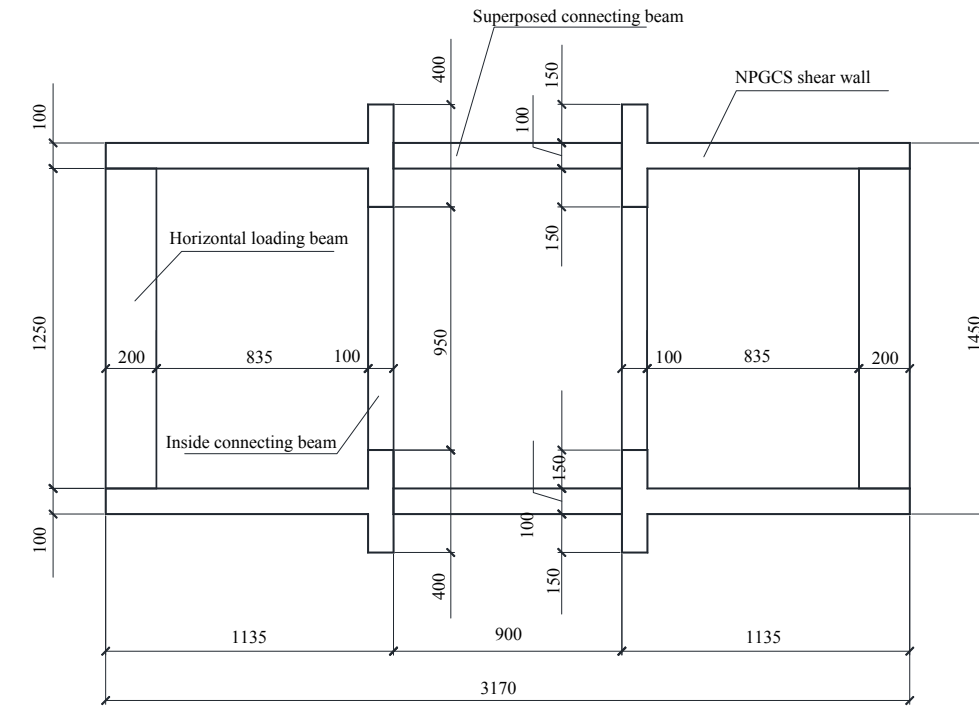
In addition to the above three design criteria, the basic length requirement of the overlapped connecting steel bars should be satisfied according to the ‘Code for design of concrete structures’ applied in China, and will be 40 times the steel bar diameter.

2.3. NPGCS properties

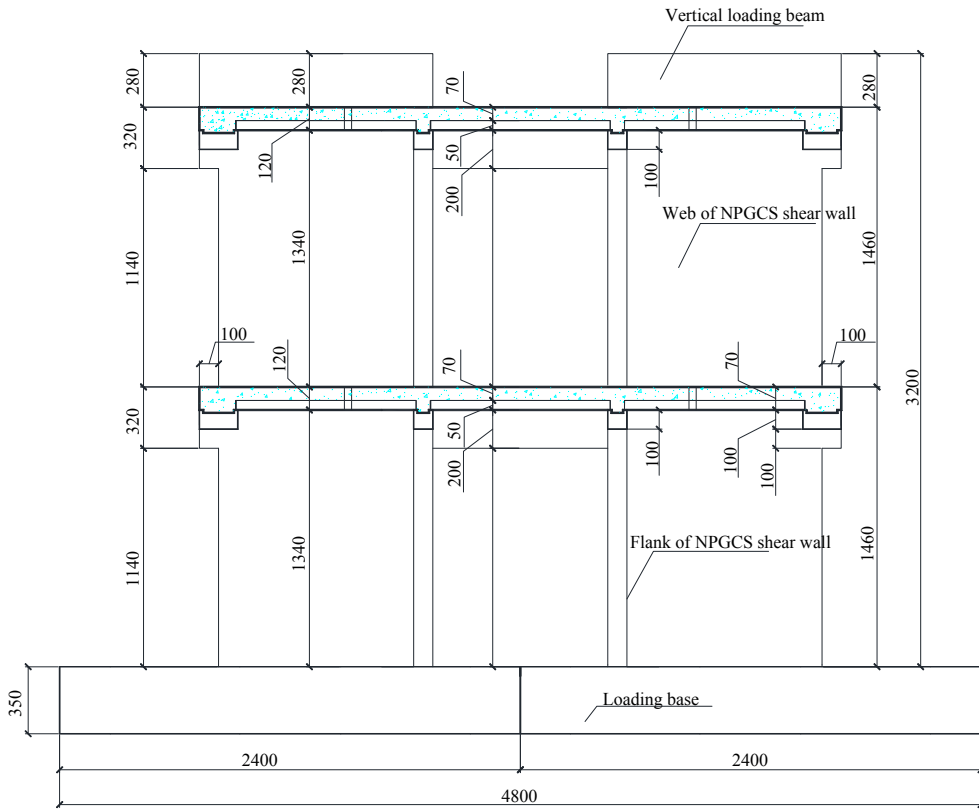
In early research, low cyclic loading experimental tests were carried out on NPGCS precast wall specimens by the author et al. [7,12], which is the pre-study of this NPGCS spatial model and financial supported from the National Science & Technology Pillar Program during the Twelfth Five-Year Plan Period of China. The experimental specimens included one cast-in-situ shear wall specimen and two NPGCS precast

shear wall specimens. The specimen design parameters were selected from the shear wall component in a high-rise residential building, and designed according to the ‘Code for seismic design of buildings’ in China. The concrete strength of the three specimens was C30 (16.5 MPa), while the strength of all reinforcement steels was HRB400 (400 MPa), including the vertical, horizontal, connection and confinement steels. The specimen sizes and steel bar configurations are illustrated in Fig. 6 and the loading setup is depicted in Fig. 7. The MTS applied a maximum lateral load of 2500 kN, and the vertical load acting on the specimen top was 750 kN, applied by two 500 kN lifting jacks. The specimen sizes and testing results are displayed in Table 1.

The strength test results from Table 1 indicate that the strength of the NPGCS precast shear wall specimens is no lower than that of the cast-in-situ specimen, including the crack, yield and ultimate strengths. The ductility coefficients of ZP-1 and ZP-2 are 5 and 6, respectively, which are 16.7% weaker than and equal to that of XJ-1, respectively, indicating that the NPGCS precast wall exhibits a close ductility. Moreover, the failure mode of the NPGCS specimens, illustrated in Fig. 8, is the bearing-shear failure, which is the same as that of the cast-



a. Plane section



b. Vertical section

Fig. 12. Sizes of NPGCS spatial model.

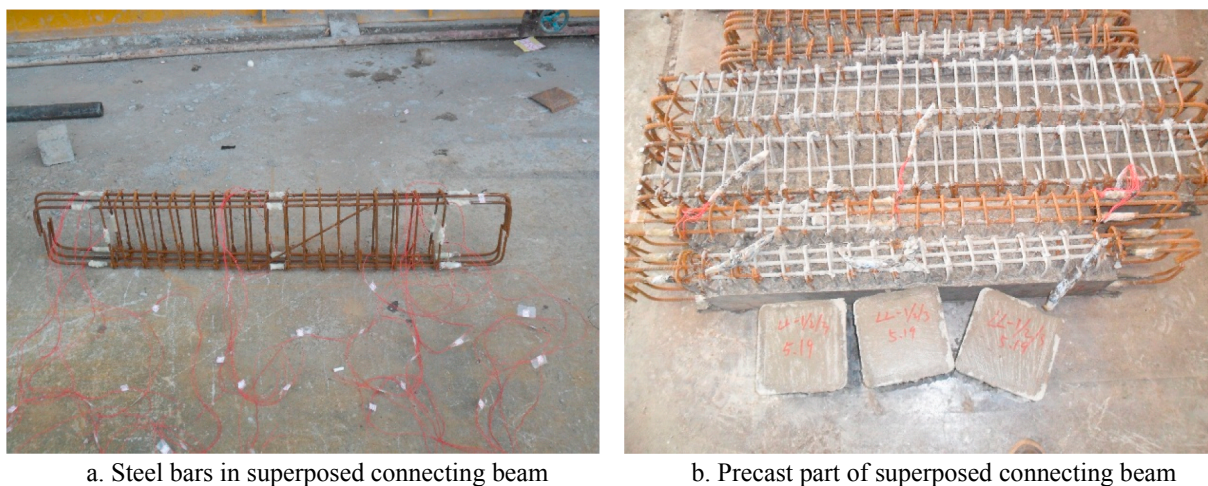


Fig. 13. Manufacturing of superposed connecting beams.



Fig. 14. Manufacturing of superposed floor slab.

in-situ specimen, with the only differences being the vertical gap opening and lateral interface slip at the precast joint interface after the vertical steels yield. Overall, it can be concluded that the mechanical properties, including the strengths and ductility, of the NPGCS are sufficient to match the ‘equal to cast-in-situ’ mechanical design requirements. However, the seismic performance of high-rise residential precast shear wall buildings is synthetically related with precast shear wall and connecting beam which is formed by the shear wall window openings. Therefore, as the subsequent study of the single NPGCS shear wall specimens, the experimental evaluation on one NPGCS spatial structure model containing precast shear wall and superposed connecting beams was carried out in this study.

2.4. NPGCS spatial model

In 2014, the NPGCS was applied to a 33-storey precast shear wall high-rise residential building in the county-level city Haimen, of the Jiangsu Province in China. The building is $26.3\text{ m} \times 15.9\text{ m}$ in plot dimensions and the structure height is 102.7 m. As the first high-rise precast residential building in China, its seismic fortification intensity is of the 7th grade, with a 0.15 g earthquake ground motion acceleration, where g is the gravity acceleration. In order to achieve superior seismic

security, a cast-in-situ construction approach was used for the bottom five floors, while the NPGCS precast shear wall technology was applied to the above 28 floors. In order to evaluate the seismic reliability of this precast high-rise residential structure, early experimental tests on single NPGCS precast walls [7,12], as mentioned in Sections 2.2 and 2.3, as well as a seismic time-history evaluation [23] for the entire precast structure, were carried out. In the seismic time-history evaluation, the labelled precast shear walls on the sixth floor, illustrated in Fig. 9, were the most important components for which the concrete material damage was serious, as shown in Fig. 10. It should be noted that the sixth floor was the key floor in this building, as the bottom five floors were cast-in-situ and the NPGCS precast shear wall technology was applied starting from the sixth floor, so the labelled precast walls in Fig. 9 should be selected from the sixth floor. Apart from this, considering that the moment is the major influencing internal force for high-rise shear wall structures, two floor heights were selected as the spatial model height for enlarging the moment influence. Finally, the NPGCS spatial model sizes were based on the most important precast shear walls illustrated in Fig. 9 from the sixth and seventh floors.

As it was limited by experimental conditions, the NPGCS spatial model was half of the real structure size. The concrete strength grade was C35. The main steel bars in the NPGCS spatial model were the HRB400 (C) grade, which was the Hot-rolled Ribbed-steel Bar with the yielding strength of 400 MPa. The 4-mm diameter HPB300 (A) grade steel bars were used as confinement steel bars, which was the Hot-rolled Plain-steel Bar with the yielding strength of 300 MPa, because the halved diameter of the 6-mm confinement steel bars in a real structure would be a seldom-used diameter of 3 mm. After determining the material strengths, based on the design criteria for the strength-equal model in the ‘Standard for test method of concrete structures’ in China, the sizes and steel bars in each component after exchange into a half-size scale are displayed in Table 2. The assembly details are illustrated in Fig. 11 and the NPGCS spatial model sizes are indicated in Fig. 12. The precast component manufacturing and the spatial model assembly are illustrated in Figs. 13–16.

2.5. NPGCS spatial model test setup

The experimental test setup is illustrated in Fig. 17. The specimen total size in the plain is $4.8\text{ m} \times 2.1\text{ m}$ with a height of 3.55 m. The specimen sizes are listed in Table 2. According to NPGCS characteristics

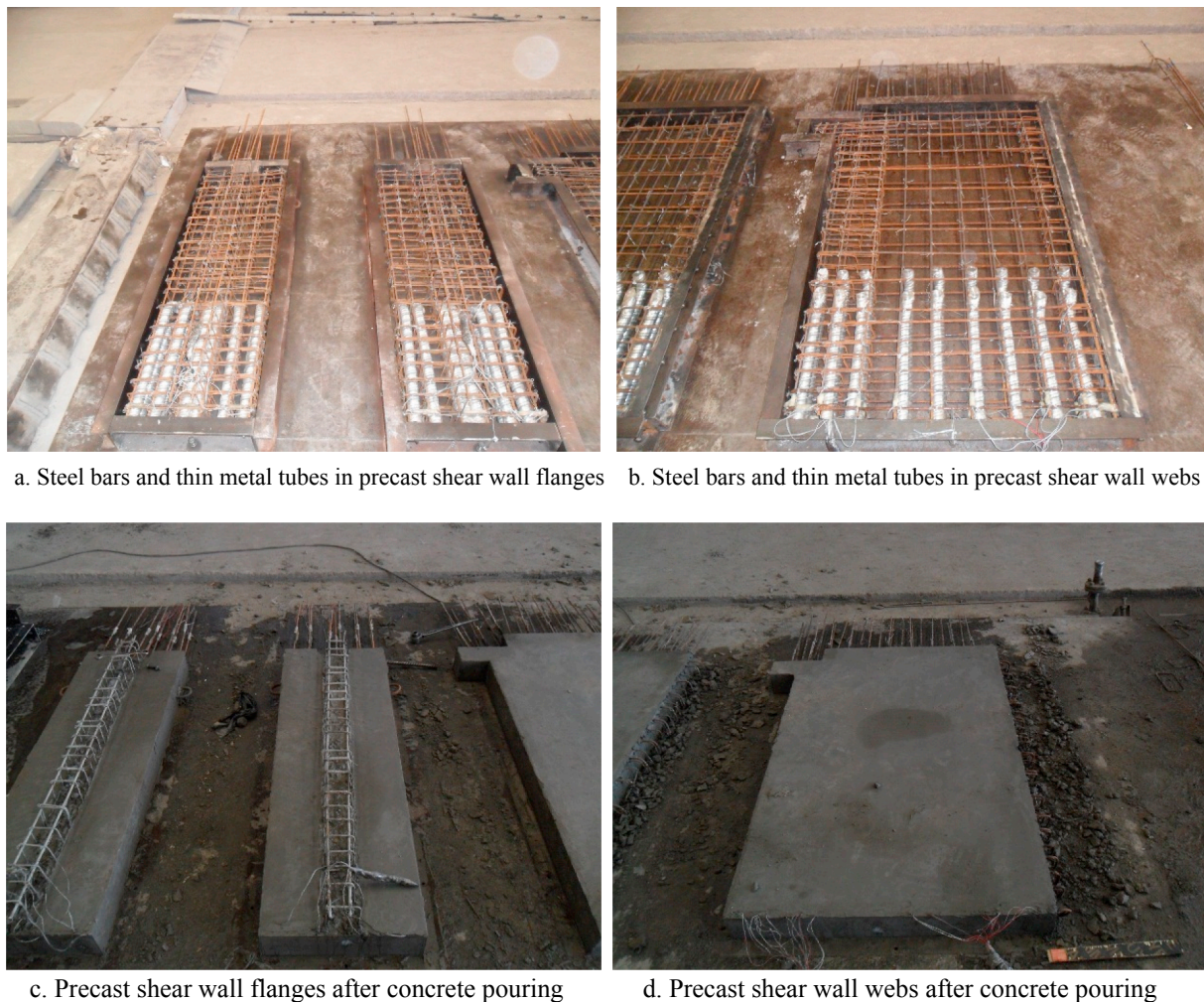


Fig. 15. Manufacturing of precast shear wall components.

and limited by loading conditions, the low cyclic reversed lateral loading test was applied using only one 2500 kN level MTS hydraulic servo system jack at the second floor of the NPGCS spatial model with 3.17 m above the ground shown in Fig. 17, because the NPGCS model was designed from a 33-storey high-rise building, in which the bending moment is so large that the influence of lateral force applied at the first floor of NPGCS spatial model in inverted triangle distribution would be very low, and also the synchronized controlling for two MTS hydraulic servo system jack would be more difficult in the test. The loading process was divided into two phases according to the ‘Specification for seismic test of buildings’ [24]: the force and displacement control phases, which is divided by the NPGCS steel bar yielding. And according to the Section 4.4 of the ‘Specification for seismic test of buildings’, during the force control phase, each step is loaded by 50 kN and circulated once, while in the displacement control phase, one yielding displacement time is applied and it is circulated three times. The loading speeds in force control phase and displacement control phase are the same. To achieve the cyclic forward and opposite loading, four 30 mm diameter screw-thread steel bars for prestressing concrete were used to form the horizontal loading connections and were only artificially screwed up without large post-tensioned stress when low pushing force was applied on the NPGCS specimen in preloading phase, shown in Figs. 17 and 18. And according to early finite element study

results for the 33-storey precast building, the design axial load ratio was 0.24, and eight 500 kN level hydraulic jacks were set at the spatial model top to apply an axial compression load of 2400 kN.

During the test, the lateral force and displacement data of NPGCS spatial model loading point were collected by the integrated force and displacement sensors in the MTS hydraulic servo system. The axial compression load was applied by eight hydraulic jacks and artificially controlled by high precision hydraulic oil gauge in every loading step. The joint interface slips were tested by dial gauges utilized at shear wall-base joint. To identify the steel bar yielding, some electric resistance strain gauges were set on steel bars crossing precast shear wall joint interface and connecting beams.

3. Experimental test results

3.1. Observational phenomena

The observational phenomena of the NPGCS spatial model are related to 12 components and 14 joint interfaces. In order to provide convenient phenomena descriptions, the names of the components and joint interfaces are indicated in Fig. 19.

(1) Cracks



a. Component assembly of first floor



b. Concrete pouring for superposed components of first floor



c. Component assembly of second floor



d. Concrete pouring for superposed components of second floor

Fig. 16. Assembly of NPGCS spatial model.

Figs. 20 and 21 illustrate the crack distributions on the shear walls and superposed connecting beams.

The first visible crack was at the end area close to joint 3 on the superposed connecting beams when the lateral load was 300 kN. With an increasing lateral load, the cracks on the superposed connecting beams continued to develop in width and length. The longitudinal steel bars in the superposed connecting beams firstly yielded at 450 kN and the concrete at the superposed connecting beams end area close to joint 3 began to be compressively damaged. Thereafter, several new cracks inclined at 45 degrees to the axial beam and serious concrete damage came into existence and gathered at the beam end area, close to joint 3. No cracks occurred in the middle span area of the superposed connecting beams. The superposed connecting beams yielded and were damaged earlier than the shear wall components.

Joint 1 first cracked when the lateral load was 350 kN. Thereafter, the precast shear walls firstly cracked at approximately 350 mm above joint 1 when the lateral load was 450 kN. It should be noted that the grouted length of the connecting steel bars was 350 mm. Theoretically, two overlapped steel bars will generate two weak sections at the overlapping ends, so the first cracks prove the existence of two weak sections at 350 mm above joint 1, and the joint 1 section caused by the overlapping of the grouted connecting steel bars and original vertical steel bars. In contrast, joint 1 is more important than the weak section

350 mm above joint 1, as it bears a larger moment.

During the early force-controlled loading phase, all of the precast shear walls cracked and extended in the horizontal direction, because the shear wall height of the two floors enlarged the moment influence. With the increased lateral load, additional new cracks came into existence and the old cracks continued to increase in length and width. After the loading process entered the displacement control phase, the existing cracks developed into an inclined direction and finally into nearly 45 degrees to the horizontal direction. The cracks were bending-shear cracks. All of the cracks on the shear walls gathered at the first floor, but no cracks were observed at the second floor, indicating that joint 1 and the first-floor shear walls are key components and additional attention should be paid to these, while joints 2, 4 and 5 remained intact during the test and can be neglected in further studies.

(2) Joint interface slips

As dial gauges are utilized to test the joint interface slips of the precast shear walls shown in Fig. 22. There were four dial gauges in total for the A, B, C and D walls, respectively, and Fig. 23 illustrates the lateral load-slips curves. As the A/B and C/D dial gauges were set at symmetrical positions in the spatial model, the A/B and C/D slips were opposite. In Fig. 23, the A and B wall slips are negative with the lateral

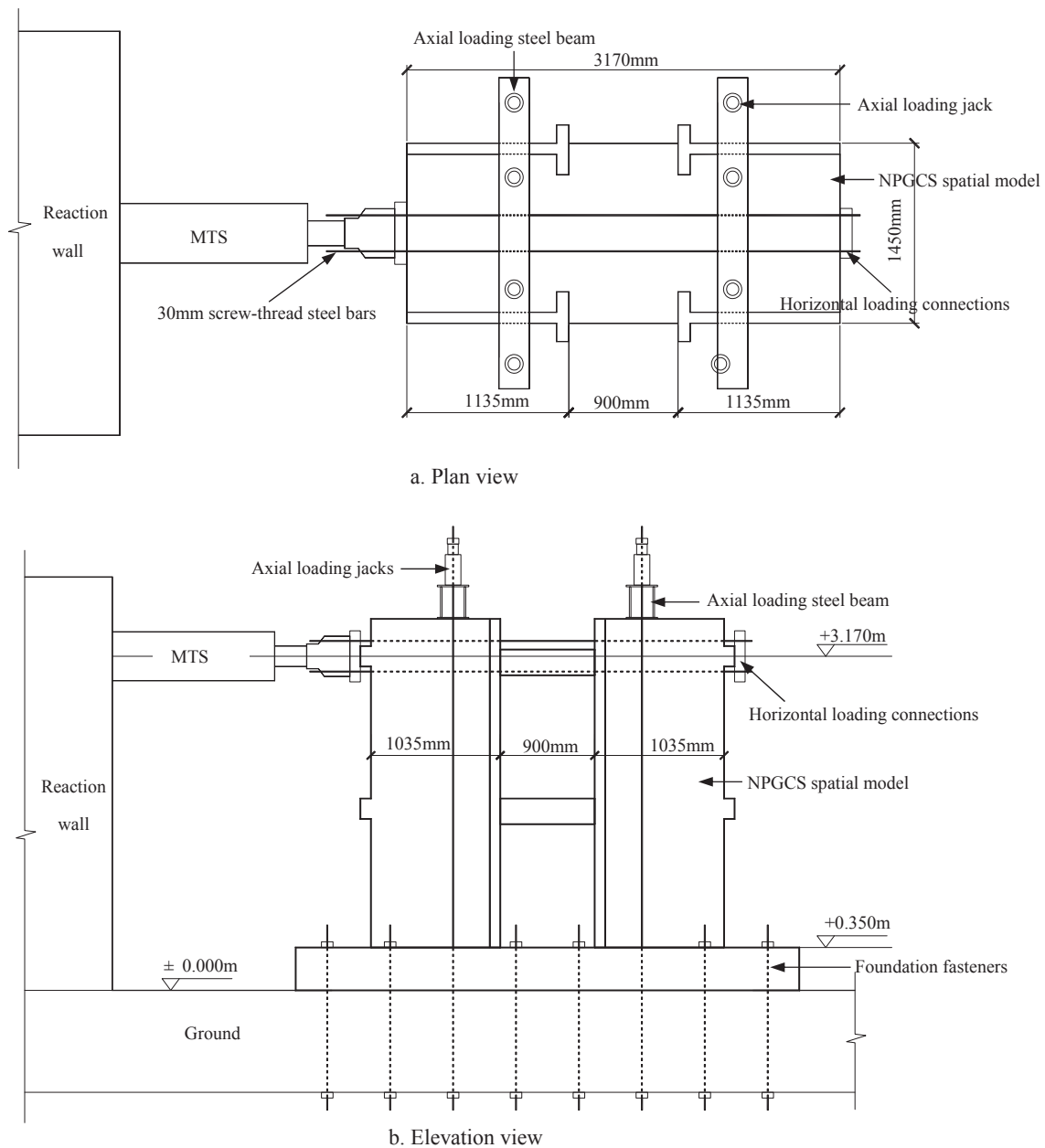


Fig. 17. Experimental test setup.

load, while the C and D wall slips are positive with the lateral load. According to the crack distributions in Fig. 21 and the joint interface slips in Fig. 23, the crack distributions on different precast walls differ according to the joint interface slips: a precast shear wall with larger interface slips, such as the A wall, has less cracks. According to early research results [25], interface slips will cause a large dowel shear stress on the connecting steel bars, which can dramatically reduce the yield strength of connecting steel bars. As a result, less stress will be transferred by connecting the steel bars to the upper precast shear wall, and the wall cracks will be reduced. Large joint interface slips will reduce the seismic properties owing to the concentrated yielding for the connecting steel bars at the joint interface, as well as reduce the ductility and seismic energy consumption.

(3) Failure mode

Figs. 24–26 illustrate the failure details of the superposed connecting beams and precast shear walls. The superposed connecting beam failure was a typical shear failure, in which the steel bars yielded and the concrete experienced serious compressive damage concentrated at the beam ends to generate two plastic hinges, while no cracks or concrete damage occurred at the beam middle span. The precast shear wall failures were typical bending-shear failures, as the two floors of the shear wall enlarged the moment-shear ratio. In the web edge of the joint 1 section, the concrete experienced severe compressive damage and several steel bars were pulled to be fractured. As part of the concentrated fracture of the steel bar at joint 1, no failure extending into the NPGCS was determined in the experimental test, successfully



Fig. 18. Test setup and specimen in reality.

proving that the NPGCS completely matched the full force-transferring requirements and joint 1 is a new weak section that should be noted.

3.2. Lateral force and top displacement

Figs. 27 and 28 illustrate the force-displacement hysteretic and skeleton curves. It can be observed that all of the curves can be divided into the elastic, elastic-plastic and failure stages. During the elastic stage, the NPGCS model top displacement maintained a linear relationship with the lateral load, and the hysteretic loop area was very small. The loop area began to enlarge after the superposed connecting beams were damaged and joint 1 was cracked, and the curves began to exhibit plastic properties. This indicated that most of the seismic energy consumption value was attributed to the plastic deformation of the shear walls, as the superposed beams were not designed properly and had already undergone serious damage when plastic deformation occurred on the shear walls. During the elastic-plastic stage, the hysteretic loop was S-shaped, and the hysteretic loop area began to enlarge significantly, becoming fuller than that in the elastic stage. During the failure stage, the hysteretic loop area approximately remained as full as that in elastic-plastic stage, so it was qualitatively proven that the seismic performance of the NPGCS spatial model in the failure stage was still effective, but the seismic performance of the NPGCS spatial model should be quantitatively supported by the energy consumption value.

3.3. Strengths

The NPGCS spatial model strengths based on the experiment, calculation according to design standards and finite element simulation are indicated in Table 3, in which the yield load and displacement were determined by the general yield moment approach used for the inconspicuous yielding curves illustrated in Fig. 29. The mechanical properties in the forward loading differed to those in the opposite loading: the forward loading yield strength, ultimate strength, and ultimate displacement were larger than those in the opposite loading. However, the forward loading yield displacement was lower than the opposite loading yield displacement. Therefore, the opposite loading

stiffness was lower than the forward loading stiffness. This is because, owing to the large loading equipment gap opening occurring when the loading process was transferred from the force control to the displacement control, the opposite loading displacement was enlarged and the opposite loading stiffness was reduced. This was also proven by the following stiffness reduction, illustrated in Fig. 30.

The experimental yield strengths of the NPGCS spatial model are 859.5 and 764.5 kN for the forward and opposite loading, respectively, which are larger than the calculated yielding strength of 767.6 kN for the cast-in-situ shear walls of the same sizes and reinforcements with the NPGCS spatial model, according to the equations in the ‘Code for design of concrete structure’ in China, which use the material design strength value and consider the superposed connecting beam influence, as indicated in Eqs. (1) and (2).

$$N \leq \frac{1}{\gamma_{RE}} \{ \alpha_1 f_c [\xi b h_0 + (b'_f - b) h'_f] + f'_y A'_s - \alpha_s A_s + N_{sw} \} \quad (1)$$

$$Ne = \frac{1}{\gamma_{RE}} \left\{ \alpha_1 f_c \left[\xi (1 - 0.5\xi) b h_0^2 + (b'_f - b) h'_f \left(h_0 - \frac{h'_f}{2} \right) \right] + f'_y A'_s (h_0 - a'_s) + M_{sw} \right\}, \quad (2)$$

where

$$e = e_i + \frac{h}{2} - a$$

$$e_i = \frac{M}{N} + e_a$$

$$N_{sw} = \left(1 + \frac{\xi - \beta_1}{0.5\beta_1\omega} \right) f'_{yc} A_{sw}$$

$$M_{sw} = \left[0.5 - \left(\frac{\xi - \beta_1}{\beta_1\omega} \right)^2 \right] f_{yw} A_{sw} h_{sw}$$

In the above, γ_{RE} is the seismic strength adjustment coefficient, and

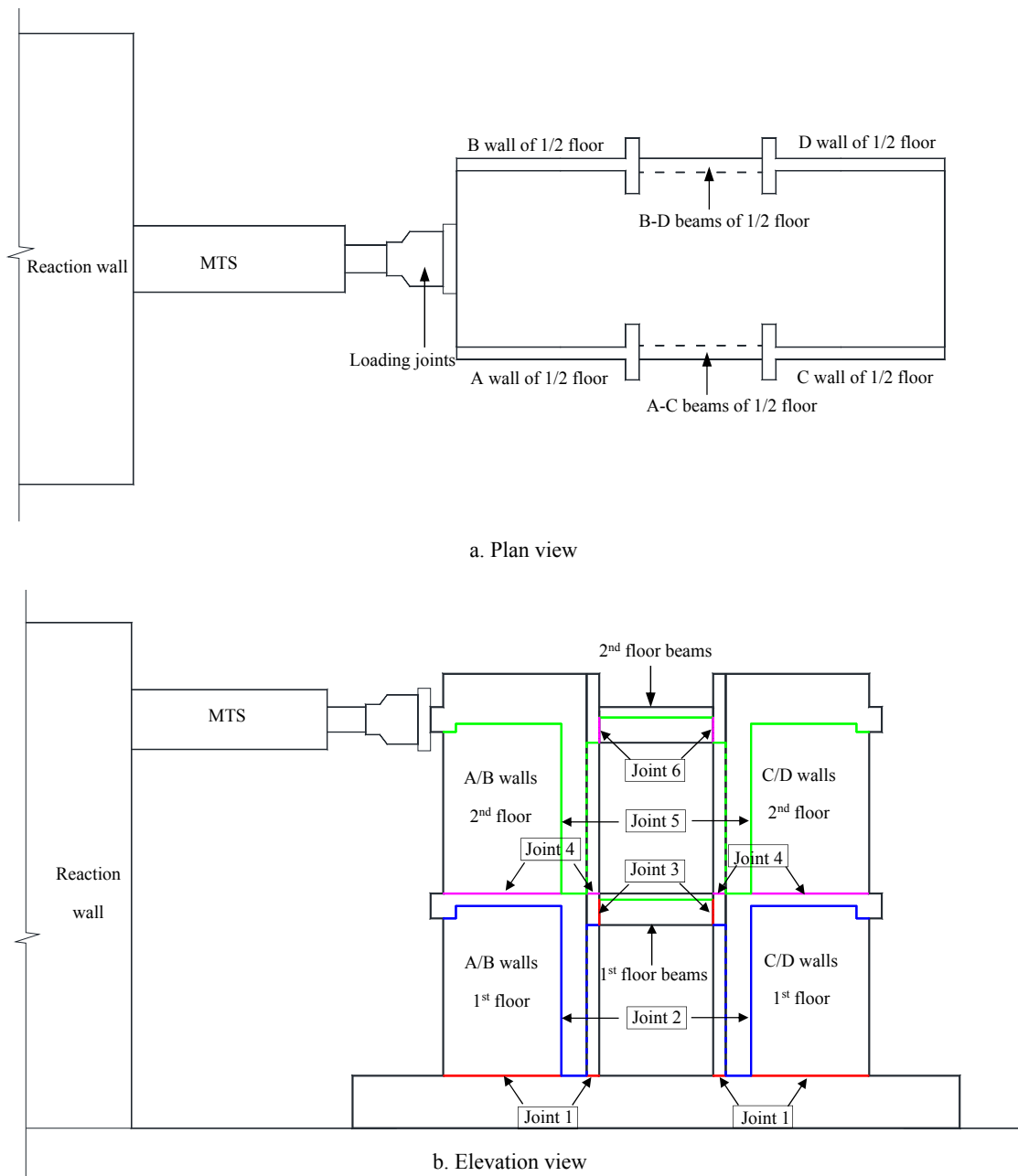


Fig. 19. Component and joint interface names. *Note: Joint 1 contains eight joints belonging to the flange and web area joints of the A/B/C/D walls on the first floor. Joint 2 contains the initial and post concrete pouring joints of the shear walls on the first floor. Joint 3 contains the beams-post concrete pouring shear wall joints on the first floor. Joint 4 contains eight parts belonging to the flange and web area joints of the A/B/C/D walls on the second floor. Joint 5 contains the initial and post concrete pouring joints of the shear walls on the second floor. Joint 6 consists of the beams-post concrete pouring shear wall joints on the second floor.*

will be 0.85 for the shear wall.

According to the results in Table 3, the forward loading yield strength is large, while the opposite strength is very close to the standard calculated design yielding strength. The ultimate strengths of the NPGCS spatial model are 1042.5 kN and 946.1 kN for the forward and opposite loading, respectively, which are higher than the ABAQUS finite element simulation strength of 927.1 for the cast-in-situ spatial model with the same sizes and reinforcements as NPGCS. All of the

yielding and ultimate strength values exceeding or not very close to those of the cast-in-situ spatial model indicate that the NPGCS connector successfully achieved effective connection properties in terms of strength and matched the seismic requirements for high-rise buildings in the 7th grade seismic fortification intensity.

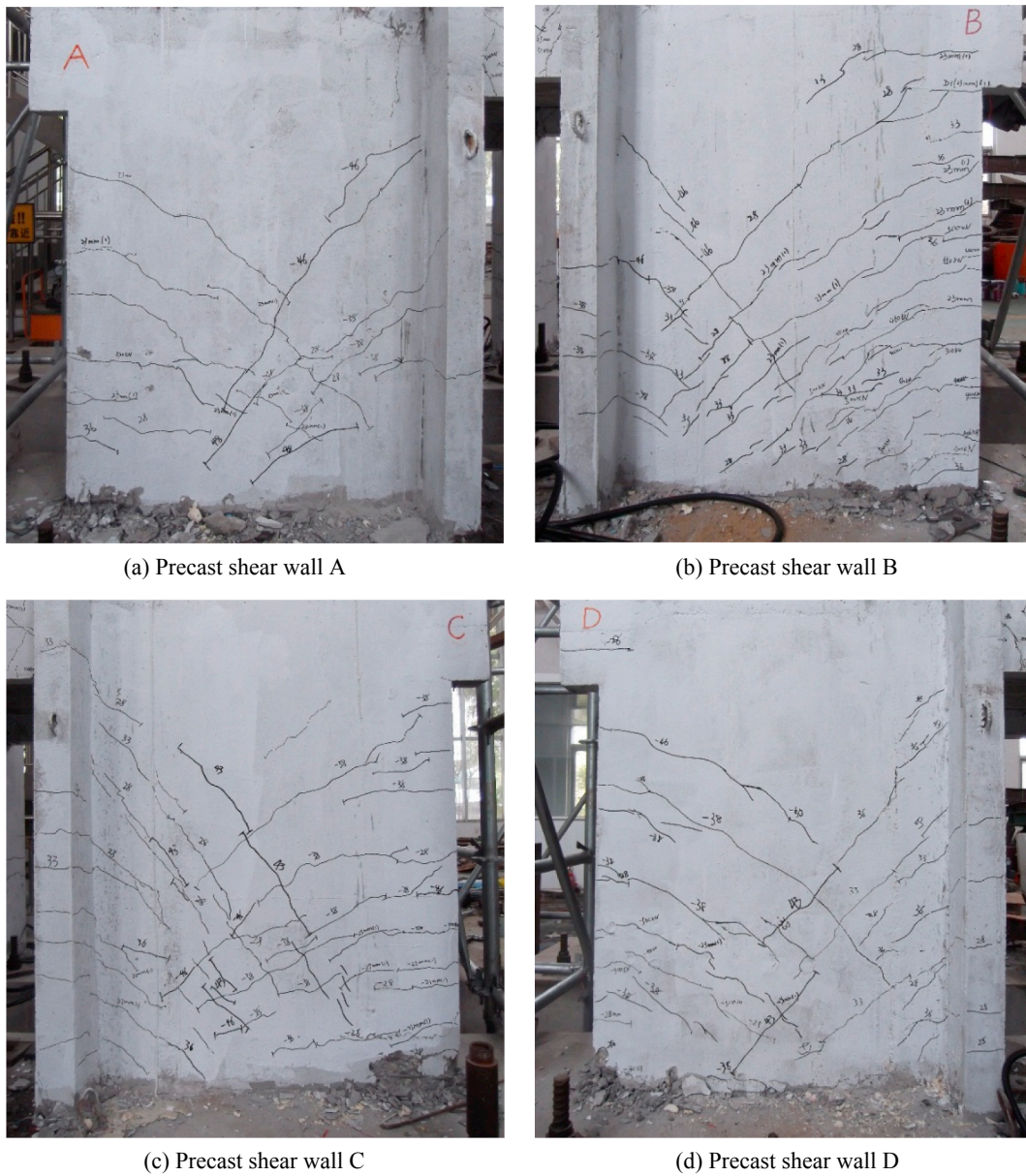


Fig. 20. Crack distributions on precast shear walls.

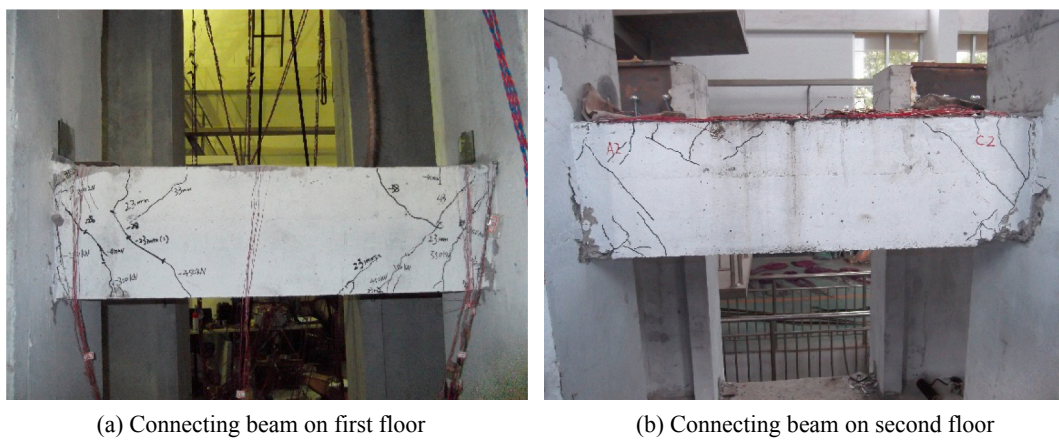


Fig. 21. Crack distributions on connecting beams.

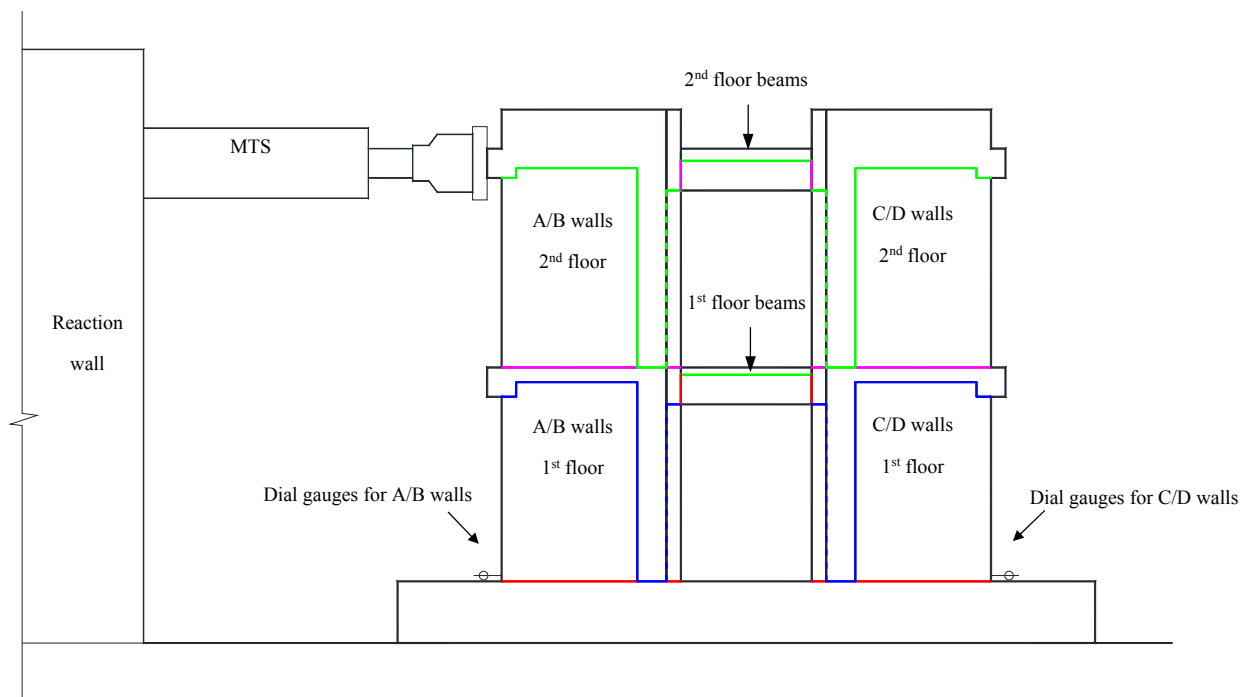


Fig. 22. Dial gauge distributions for joint interface slip of precast shear walls.

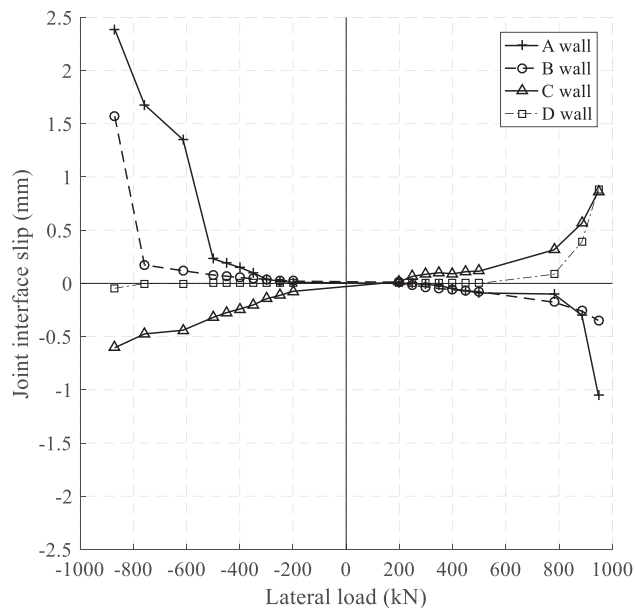


Fig. 23. Lateral load-slip curves for precast shear walls.

3.4. Displacement and ductility

The displacement and ductility results are displayed in Table 4, where it can be observed that the ductility factors of the NPGCS spatial model were 1.95 and 1.55 for the forward and opposite loading, respectively, which were obtained by dividing the displacement at the ultimate strength point into the yield displacement. For the same reason of the large loading equipment gap opening in the loading process

exchange, the opposite loading displacement, particularly during the early elastic stage, was enlarged because of the influence from the equipment gap opening, which can also be proven by the stiffness reduction illustrated in Fig. 30. Moreover, as the height-width ratio of the shear walls was 2.32 and the design axial load ratio was 0.24, the ductility factors were relatively low. However, owing to the high strength for the shear walls with a low height-width ratio and high axial load ratio, the seismic performance cannot be simply evaluated by the ductility factor. Therefore, the energy consumption value needs to be calculated to evaluate the seismic performance.

3.5. Stiffness reduction

Fig. 30 illustrates the stiffness reduction curve of the NPGCS spatial model. During the force loading phase, the stiffness reduction was very low and continued to increase with the loading. The stiffness reduction became obvious once the lateral displacement reached ± 5 mm with a ± 350 kN lateral load. During the displacement loading phase, the stiffness reduced rapidly, indicating that additional plastic deformation and damage occurred. When the lateral displacement reached ± 10 mm, with the lateral load exceeding ± 550 kN, the opposite loading stiffness was significantly reduced owing to the loading equipment gap opening, corresponding to the yield displacement differences in Table 4. However, following this significant stiffness reduction, the stiffness reduction trends for the forward and opposite loading were almost equal, indicating that the effects of the loading equipment gap opening were weak during the displacement loading phase.

3.6. Energy consumption value

The energy consumption value was calculated by means of the numerical calculation method, and Fig. 31 illustrates the energy consumption value-displacement curve. During the force loading phase, the

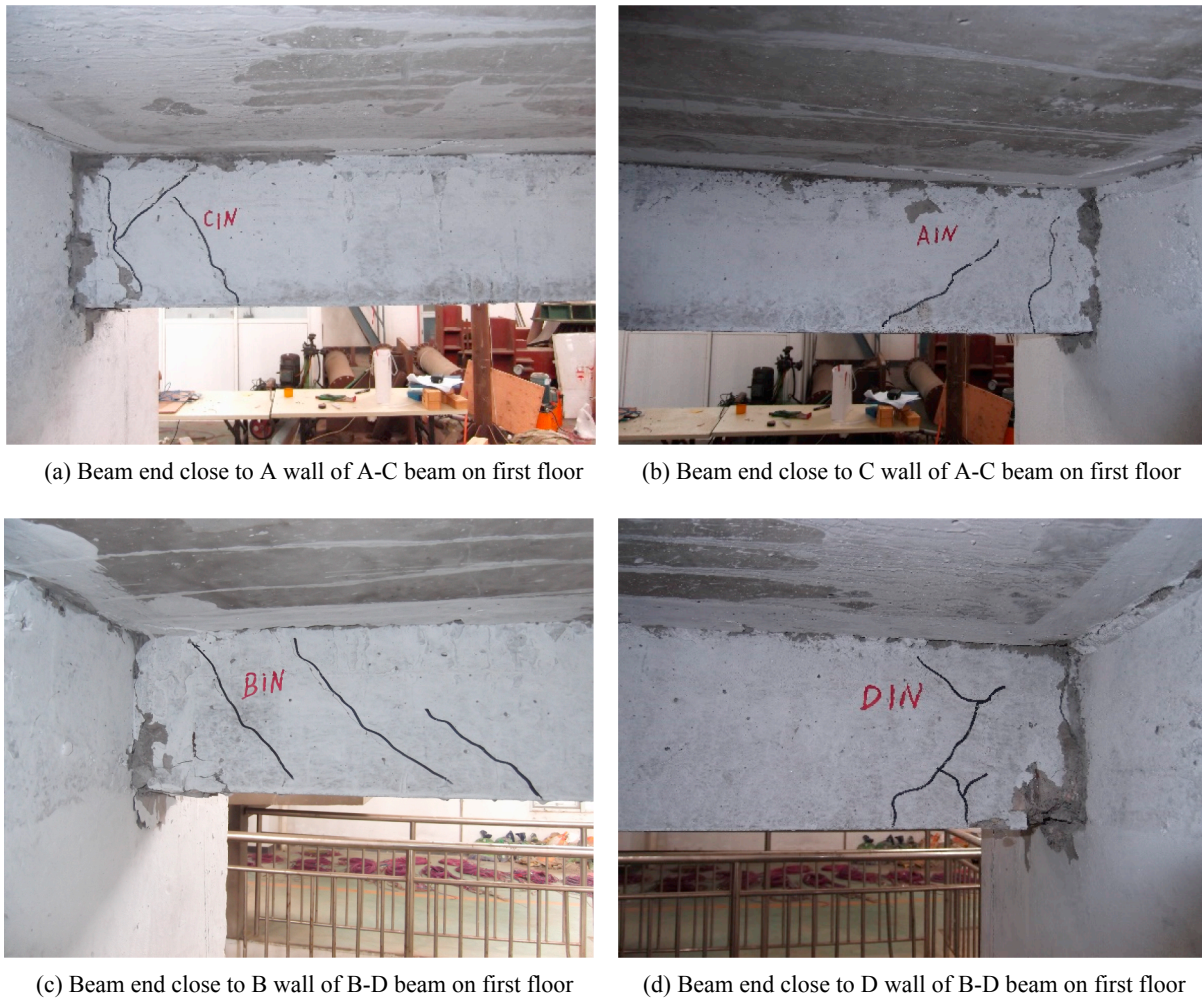


Fig. 24. Damage of first floor superposed connecting beams.

energy consumption value was very low, even after the steel bar in the superposed connecting beams yielded at $350 \text{ kN} / \pm 5 \text{ mm}$. The plastic deformations of the yield steel bars in the superposed connecting beams had little effect on the entire spatial model energy consumption. Therefore, the mechanical properties of the superposed connecting beams were not very effective and should be noted in future precast shear wall design. During the displacement loading phase, as the steel bars in the precast shear walls continued to yield gradually, the energy consumption value continued to increase significantly with an increase in lateral displacement. This indicates that the plastic deformation of the connecting steel bars and concrete damage in the precast shear wall contributed the majority of the energy consumption. The largest energy consumption values reached 11.71 and 11.41 kN·m with displacements of 48.23 and 47.37 mm, for the forward and opposite loading, respectively. The maximum energy consumption values were observed during the failure stage when the spatial model strength had declined, indicating that the NPGCS spatial model still exhibited a certain seismic energy consumption ability in the failure stage.

Fig. 32 is the equivalent viscous damping coefficient-displacement curve, which was calculated by Eq. (3) according to the ‘Specification for seismic test of buildings’ [24] and the area are illustrated in Fig. 33. It can be found that the equivalent viscous damping coefficient kept

increasing in the failure stage, proving the NPGCS has a certain seismic energy consumption ability when shear walls are seriously damaged in failure stage. But as the shear wall components in NPGCS spatial model has a relative low shear span ratio of 2.72 and high axial compression ratio of 0.2, the energy consumption value may be seriously limited and the equivalent viscous damping coefficient is lower than 0.1.

$$\zeta_{\text{eq}} = \frac{1}{2\pi} \cdot \frac{S_{(ABC+CDA)}}{S_{(OBE+ODF)}} \quad (3)$$

In the above, ζ_{eq} is the equivalent viscous damping coefficient

4. Conclusions

Based on the experimental test on the NPGCS spatial model, the following conclusions related to the seismic properties can be obtained.

- (1) The superposed connecting beams cracked at the beam end area, close to the beams-post pouring concrete shear wall joints. The precast shear walls firstly cracked at the precast shear wall joints (joint 1) and at a height of approximately 350 mm above joint 1 after the steel bars in the superposed connecting beam yielded, proving the existence of two new weak sections at the grouted



Fig. 25. Damage of second floor superposed connecting beams.

connecting steel bar ends.

- (2) The crack distributions on the different precast walls varied with the joint interface slips: precast shear walls with larger interface slips will exhibit less cracks. This is because interface slips will cause dowel shear stress and a dramatic yield strength reduction on the grouted connecting steel bars; thus, joint interface slips should be noted.
- (3) The NPGCS spatial model failure consisted of the superposed connecting beam failure, precast shear wall concrete damage and grouted connecting steel bar fractures at the joint interface. The failure of the superposed connecting beams was typical shear failure, and two plastic hinges were generated at the beam ends. The precast shear wall failure was bending-shear failure, in which the concrete experienced serious compressive damage and several steel bars were pulled to fracture. All of the steel bar fractures gathered at the joint interfaces but no NPGCS connector failure occurred, which successfully proved the mechanical reliability of the NPGCS and weak failure section at the joint interface.
- (4) A comparison of the experimental strengths of the NPGCS spatial model with the equation-calculated and finite element simulated strengths of the cast-in-situ spatial model with the same sizes and design parameters as the NPGCS spatial indicated that the NPGCS

connector successfully achieved effective connection properties in terms of strength and matched the seismic requirements for high-rise buildings in the 7th grade seismic fortification intensity.

- (5) The NGPCS spatial model was based on a real high-rise residential building, so the axial load was high and the height-width ratio of the precast shear walls was low. As a result, the NGPCS spatial model has low ductility properties.
- (6) The energy consumption value of the NPGCS spatial model during early loading was very low, and even the steel bars in the superposed connecting beams yielded very early. This is because the superposed connecting beams were not properly designed, leading to insufficient properties. Therefore, it is suggested that the connecting beams in the high-rise precast shear wall buildings should be investigated further and properly designed.
- (7) During the failure stage, the energy consumption value of the NPGCS spatial model continued to increase, even when the strength declined, but as limited by shear span ratio and axial compression ratio of the shear wall components. Thus, the seismic performance was effective and most of the energy consumption was attributed to the shear wall steel bars yielding and concrete damage.



(a) Precast shear wall A



(b) Precast shear wall B



(c) Precast shear wall C



(d) Precast shear wall D

Fig. 26. Damage of precast shear walls at base position.

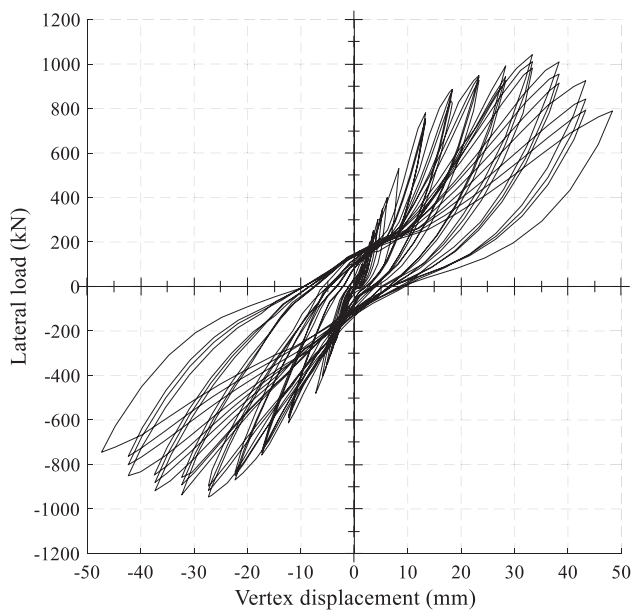


Fig. 27. Force-displacement hysteretic curve.

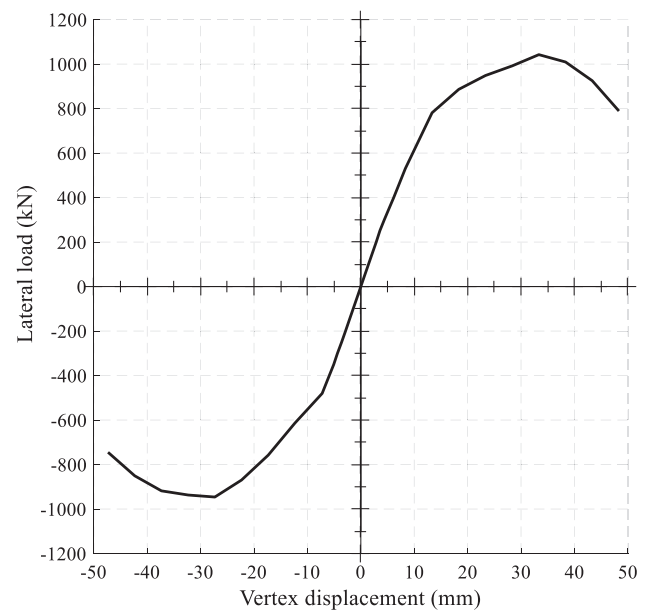


Fig. 28. Force-displacement skeleton curve.

Table 3
Strengths of NPGCS spatial model.

	Experimental crack load (kN)	Experimental yield load (kN)	Experimental ultimate load (kN)	Equation calculated strength (kN)	Finite-element simulated strength (kN)
Forward	300	859.4	1042.5	790.2	927.1
Opposite	300	764.5	946.1		

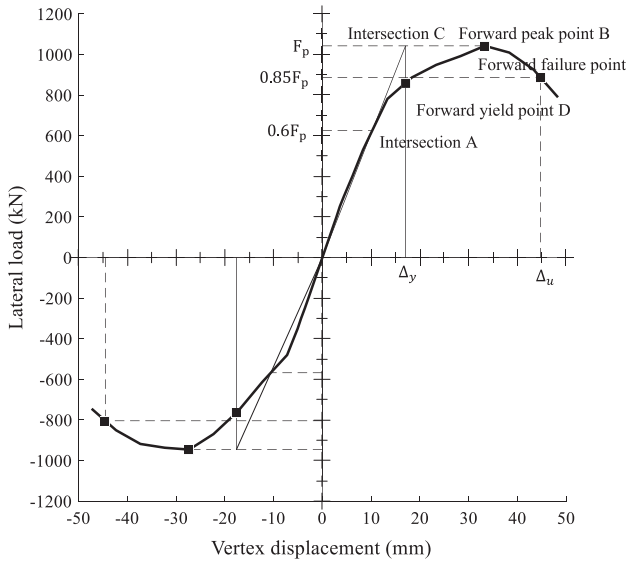


Fig. 29. General yield moment approach to determine mechanical key points.

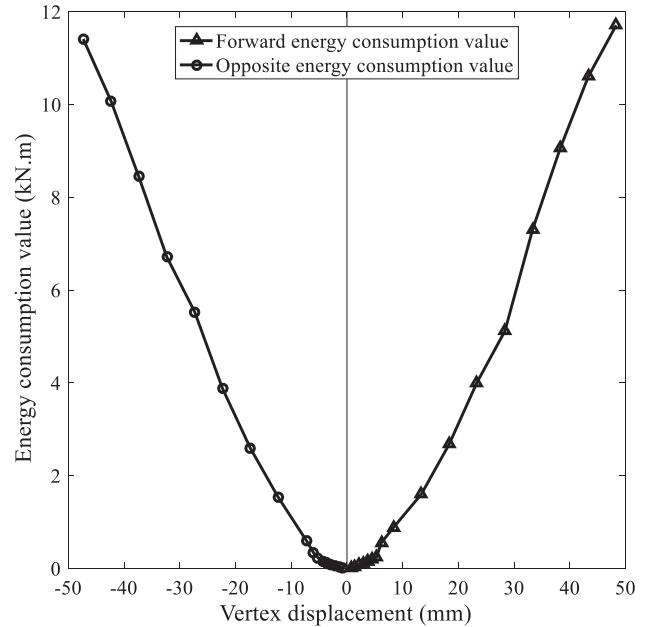


Fig. 31. Energy consumption value-displacement curve of NPGCS spatial model.

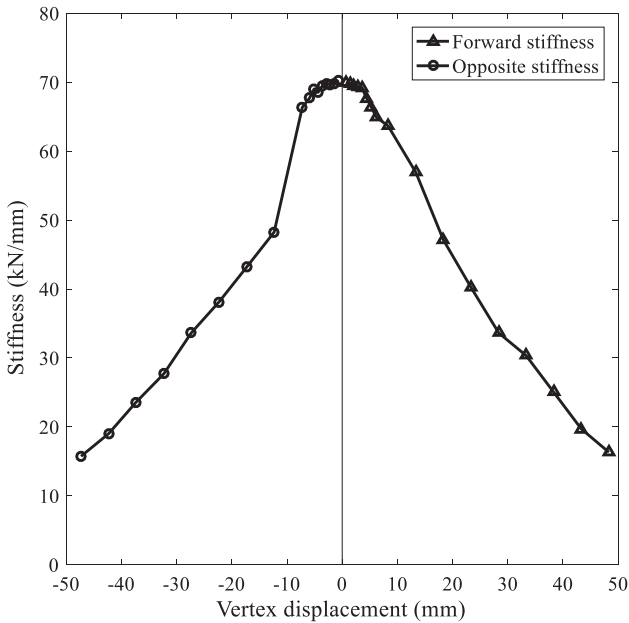


Fig. 30. Stiffness-displacement curve of NPGCS spatial model.

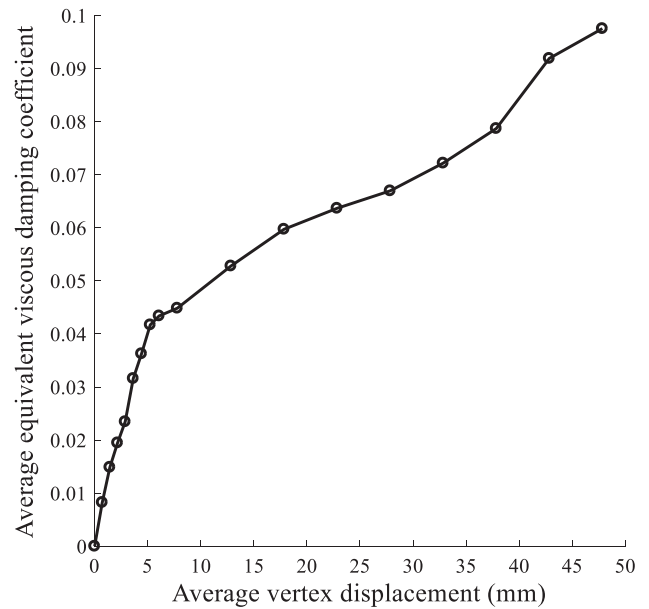


Fig. 32. Equivalent viscous damping coefficient-displacement curve of NPGCS spatial model.

Table 4
Displacement and ductility values of NPGCS spatial model.

	Yield displacement (mm)	Ultimate displacement (mm)	Failure displacement (mm)	Ductility factor
Forward	17.06	33.34	44.77	1.95
Opposite	17.64	27.34	44.53	1.55

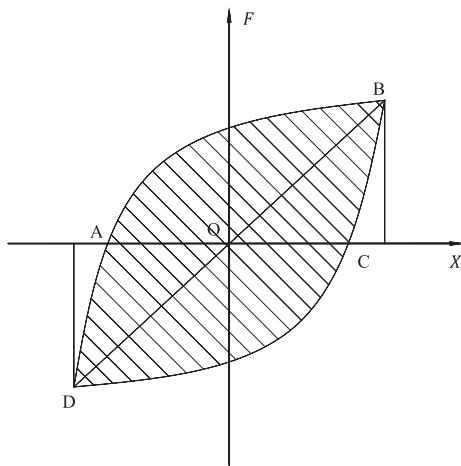


Fig. 33. Equivalent viscous damping coefficient calculation areas.

Acknowledgement

The financial support from the National Science & Technology Pillar Program during the Twelfth Five-Year Plan Period of China (Grant No. 2011BAJ10B03) is acknowledged. Moreover, this work was supported by the National Natural Science Foundation for Young Scientists of China (Grant No. 51708260) and the University Natural Science Foundation of Jiangsu Province Government (Grant No. 16KJB560003).

References

- [1] Chen J, Su Y. Prefabricated concrete shear wall structure and its connecting technology. *World Earthq Eng J* 2013;29(1):38–48.
- [2] Belleri A. Displacement based design for precast concrete frames with not-emulative connections. *Eng Struct J* 2017;2017(141):228–40.
- [3] Musselman E, Fournier M, Mcalpine P, Sritharan S. Behavior of unbonded post-tensioning monostrand anchorage systems under short duration, high amplitude cyclical loading. *Eng Struct J* 2015;104(December):116–25.
- [4] Zhang W, Qian J, Yu J, Qin H, Liu G. Tests on seismic behavior of precast shear walls with cast-in-situ boundary elements and vertical distributed reinforcements spliced by a single row of steel bars. *China Civil Eng J* 2012;45(10):89–97.
- [5] Qian J, Yang X, Qin H, Peng Y, Zhang J, Li J. Tests on seismic behavior of pre-cast shear walls with various methods of vertical reinforcement splicing. *J Build J* 2011;32(06):51–9.
- [6] Zheng Y, Guo Z. Experimental study and finite element analysis on behavior of deformed gout-filled pipe splice. *J Build J* 2016;37(03):94–102.
- [7] Wu D, Liang S, Guo Z, Xiao Q. Bending bearing capacity calculation of the improved steel grouted connecting precast wall. *J Harbin Instit Technol J* 2015;47(12):112–6.
- [8] Hu W, Zhai X, Jiang H. Study on seismic performance and construction measures optimization of precast fabricated RC integration shear wall. *J Build J* 2016;37(08):1–10.
- [9] Jiang H, Zhang H, Liu W, Yan H. Experimental study on plug-in filling hole for steel bar anchorage of the PC structure. *J Harbin Instit Technol J* 2011;43(4):28–31.
- [10] Chen Y, Liu J, Guo Z, Zhang J. Test on seismic performance of precast shear wall with reinforcements grouted in holes and spliced indirectly in horizontal connections. *J Harbin Instit Technol J* 2013;45(6):83–9.
- [11] Wang D, Lv X, Lu W. Experimental study on seismic performance of precast concrete shear walls with joint connecting beam. *J Build J* 2013;34(10):1–11.
- [12] Wu D, Liang S, Guo Z, Zhu X, Fu Q. The development and experimental test of a new pore-forming grouted precast shear wall connector. *KSCE J Civil Eng J* 2015;20(4):1462–72.
- [13] Yang H, Omidalizrandi M, Xu X, Neumann I. Terrestrial laser scanning technology for deformation monitoring and surface modeling of arch structures. *Compos Struct J* 2017;169:173–9.
- [14] Yang H, Xu X, Xu W, Neumann I. Terrestrial laser scanning-based deformation analysis for arch and beam structures. *IEEE Sensors J* 2017;17:4605–11.
- [15] Yang H, Xu X, Neumann I. Deformation behavior analysis of composite structures under monotonic loads based on terrestrial laser scanning technology. *Compos Struct J* 2017;183:594–9.
- [16] Yang H, Xu X, Neumann I. Laser scanning-based updating of a finite-element model for structural health monitoring. *IEEE Sensors J* 2016;16:2100–4.
- [17] Tang B, Zhang F, Wang Y, Wang F. Effect of pre-stressed cable on pre-stressed mega-braced steel frame. *Struct Eng Mech J* 2016;59(2):327–41.
- [18] Ling JH, Abd Rahman AB, Ibrahim IS, Hamid ZA. Behaviour of grouted pipe splice under incremental tensile load. *Construct Build Mater J* 2012;2012(33):90–8.
- [19] Sayadi AA, Abd Rahman AB, Bin JMZ. The relationship between interlocking mechanism and bond strength in elastic and inelastic segment of splice sleeve. *Construct Build Mater J* 2014;55(3):227–37.
- [20] Moosavi M, Jafari A, Khosravi A. Bond of cement grouted reinforcing bars under constant radial pressure. *Cement Concrete Compos J* 2005;27(11):103–9.
- [21] Saatcioglu M, Razvi SR. Strength and ductility of confined concrete. *J Struct Eng J* 1992;118(6):1590–610.
- [22] Wu D, Liang S, Guo Z, Zhu X. The dynamic elastic-plastic time history analysis of precast high-rise shear wall structure. *Construct Technol J* 2014;22:15–9.
- [23] Wang S, Lai J-W, Matthew J, Schoettler B, Mahin Stephen A. Seismic assessment of existing tall buildings: a case study of a 35-story steel building with pre-Northridge connection. *Eng Struct J* 2017;2017(141):624–33.
- [24] JGJ/101-2015. Specification for seismic test of buildings. Beijing: Published by China Architecture & Building Press; 2015.
- [25] Wu D, Liang S, Guo Z. Flexural capacity calculation approach for precast grouted shear wall influenced by joint interface displacements. *Adv Mater Sci Eng J* 2015.